Out-of-time-order correlators at infinite temperature: Scrambling, Order and Topological Phase Transitions

Ceren B. Dağ,[1,*] L.-M. Duan,[2] and Kai Sun[1]

[1] *Department of Physics, University of Michigan, Ann Arbor, Michigan 48109, USA*
[2] *Center for Quantum Information, IIIS, Tsinghua University, Beijing 100084, PR China*

(Dated: June 13, 2019)

We report a numerical observation where the infinite-temperature out-of-time-order correlators (OTOCs) directly probe quantum phase transitions at zero temperature. This is in direct contrast to common intuition where quantum effects are washed away by strong thermal fluctuations at high temperature. We compare numerical results with exact analytic solutions and find that the effect is not a coincidence. Instead, it is generic and highly robust as long as the underlying system can be mapped to a 1D Majorana chain. Using the Majorana basis, we find that this is a topological phenomenon, where infinite-temperature OTOCs probe zero temperature topological phases via the detection of the topological degeneracy in the entire spectrum. This insight leads to a new family of interacting and nonintegrable systems whose dynamics do not show scrambling. Our results reveal an interesting interplay between topological order and information scrambling, suggesting new ways to utilize the scrambling of quantum many-body systems.

arXiv:1906.05241v1 [quant-ph] 12 Jun 2019

I. INTRODUCTION

Out-of-time-order correlators (OTOCs) have become a widely-appreciated tool to measure the correlation build-up in space and time, and hence quantitatively characterize information scrambling in interacting many-body systems [1–5]. Started off as a theoretical tool to understand quantum information in a black hole [6, 7] its impact quickly expanded to a wide variety of subjects including but not limited to: quantum chaos [8–12], many-body localization [3, 10, 13–15], quantum integrability [9, 12, 16, 17], quantum criticality [18] and recently symmetry-breaking quantum phase transitions [19, 20].

An OTOC at infinite temperature $\beta = 1/T = 0$ is defined as,

$$\begin{aligned} F(t) &= \mathrm{Tr}\left(W^\dagger(t)V^\dagger W(t)V\right), \\ &= \frac{1}{M}\sum_{n=1}^{M}\left\langle\psi_n|W^\dagger(t)V^\dagger W(t)V|\psi_n\right\rangle, \\ &\approx \left\langle\psi_h|W^\dagger(t)V^\dagger W(t)V|\psi_h\right\rangle, \end{aligned} \tag{1}$$

where W and V are set as local operators. In the second line, we sum over a complete basis of the Hilbert space of dimension M, while in the third line, we use a random state $|\psi_h\rangle$ drawn from the Haar measure [15, 21] to approximate $\beta = 0$ infinite-temperature state [22].

In this paper, we observe in multiple model systems a sharp change in the saturation value of the infinite-temperature OTOC, $\bar{F}$, if W and V are chosen to be degrees of freedoms localized near the edge of the system. The location of this jump coincides with the phase boundary of the corresponding quantum phase transition if the same system is cooled down to zero temperature. It is worthwhile to emphasize that the infinite temperature OTOCs are effective tools for detecting chaos where the entire energy spectrum is needed [8–12, 15]. Hence it is surprising and highly not obvious that this correlator can also directly probe zero temperature physics of the ground state, such as quantum phase transitions. Let us first lay out one example to motivate our study. We consider a 1D XXZ chain,

$$H = J\sum_i\left(\sigma_i^x\sigma_{i+1}^x + \sigma_i^y\sigma_{i+1}^y + \frac{J_z}{J}\sigma_i^z\sigma_{i+1}^z\right). \tag{2}$$

At $T = 0$, the model has three quantum phases separated by two quantum phase transitions both between a gapped Ising phase and a critical XY-phase where the spectrum is gapless [23].

We employ Haar-distributed random states $|\psi_h\rangle$ and obtain Fig. 1 for various cases of the XXZ model. Due to its intrinsic symmetry, the $J_z > 0$ region of this model can be mapped exactly to $J_z < 0$, and vice versa. Therefore, OTOCs at infinite-temperature only depend on the absolute value of J_z. We observe a non-zero minimum signal in the XY-phase whereas the OTOC monotonically increases in the Ising phases ($|J_z/J| > 1$) approaching to $\bar{F} \sim 1$ as $|J_z| \to \infty$ when the spin operators at the edge of the chain $W = V = \sigma^z_{\mathrm{edge}}$ are used (blue-circles line). However, when the periodic boundary condition is set (yellow diamonds line) or a spins in the bulk of the chain $W = V = \sigma^z_{\mathrm{bulk}}$ are chosen (green left-pointing arrows), the OTOC does not really differentiate between the two phases, because the transition point is smoothed out consistent with predictions from Ref. [19]. Therefore, for bulk degrees of freedom or a closed system without boundary, the infinite-temperature OTOCs are featureless and do not reveal any information about zero-temperature quantum phases or phase transitions. Based on our numerical observation, we ask two questions: *What is the underlying physics that lets the out-of-time-order correlator at infinite temperature be accurately sensitive to the ground state physics and capture the phase transition? Is this a generic feature?*

* cbdag@umich.edu

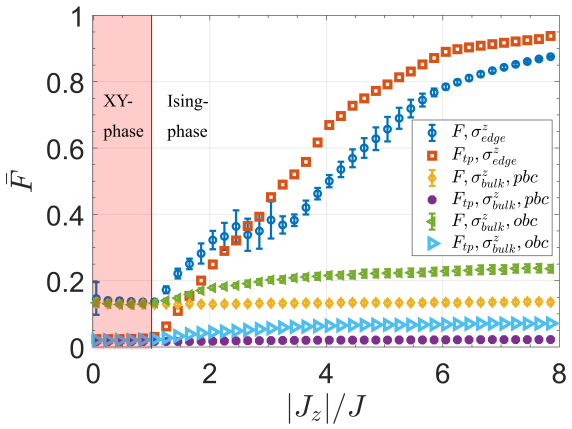

FIG. 1. Long-time average of OTOC for XXZ model for edge-spin operators $W = V = \sigma^z_{\text{edge}}$ in blue circles and its (later explained) degenerate subspace contributions in orange squares; for bulk-spin operators σ^z_{bulk} with periodic boundary chain (pbc) in yellow diamonds and its degenerate subspace contributions in purple hexagons; with open boundary chain (obc) in green left-pointing arrows and the degenerate subspace contributions in light-blue right-pointing arrows. System size is $N = 14$ and the time of averaging is $t = 800$ [1/J].

It turns out that the observed boundary effect is not an accident. Instead, it is the key to understand the relation between the information scrambling at infinite temperature and the quantum phases at zero temperature. We find that this phenomenon arises in any system as long as the system can be exactly mapped to a Majorana chain (i.e. a 1D superconductor) and through this mapping, the quantum phase transition is mapped to a topological phase transition (TPT). Hence the edge OTOCs are in fact detecting the presence/absence of the Majorana zero-energy modes. Previously, the OTOC of the integrable Ising model [16] and XX-chain [24] are analytically studied, which required periodic boundary conditions [25] and hence double-OTOCs [16, 24]. Our study indicates that OTOCs of edge operators contain new information, which is not accessible by the bulk operators. This is one key observation of our manuscript. Furthermore, the observation is highly robust where the qualitative features remain invariant even if the extra terms are introduced to the Hamiltonian to break the integrability and/or symmetries.

This counter-intuitive result hints to a deep and fundamental connection between information scrambling and topological order regardless of temperature. In addition, it opens up new avenues to dynamically detect and study topological phases through utilizing information scrambling as an order parameter. The dynamical detection of topological order has been under intensive investigation in terms of different dynamical quantities, e.g. bulk observables [26], two-time correlators [27], survival probabilities [28] of zero-energy modes. In addition to that, the topological insulators and superconductors have been studied [29–33] and classified [34] according to their non-equilibrium dynamics rather in an analogy to the classification tables for topological states of matter [35] superposed with the notion of dynamical quantum phase transitions [36–38]. Thus, understanding if the information scrambling has fundamental restrictions when topological order exists is a puzzle left at the intersection of many sub-fields.

In Sec. II, we are going to detail our numerical observation around its corresponding Majorana chain and discuss about the connection between infinite temperature scrambling and $T = 0$ topological order with quantitative arguments. Later in the section, we are going to show how the topological order is encoded in the saturation regime of OTOCs. In Sec. III and IV, we discuss the robustness of this relation via breaking the integrability and changing the boundary conditions. We will also demonstrate that the relation does emerge at any temperature.

II. TOPOLOGICAL EDGE PHYSICS ENCODED IN THE OUT-OF-TIME-ORDER CORRELATORS

A. XXZ Model in Majorana Basis

We rewrite the Hamiltonian of the XXZ model in the Majorana basis in a rotated frame:

$$H = J\sum_i \left[\left(1-2c_i^\dagger c_i\right)\left(1-2c_{i+1}^\dagger c_{i+1}\right) - \left(c_i + c_i^\dagger\right)\left(c_{i+1} - c_{i+1}^\dagger\right) + \frac{J_z}{J}\left(c_i - c_i^\dagger\right)\left(c_{i+1} + c_{i+1}^\dagger\right)\right], \tag{3}$$

where we applied Jordan-Wigner (JW) transformation via the mapping [25],

$$\begin{aligned}
\sigma_i^z &= -\prod_{j<i}\left(1-2c_j^\dagger c_j\right)\left(c_i + c_i^\dagger\right), \qquad (4)\\
\sigma_i^x &= 1-2c_i^\dagger c_i,\\
\sigma_i^y &= -i\prod_{j<i}\left(1-2c_j^\dagger c_j\right)\left(c_i - c_i^\dagger\right).
\end{aligned}$$

Now we write Eq. 3 in terms of Majorana fermions defined as $a_{2j-1} = c_j + c_j^\dagger$ and $a_{2j} = -i\left(c_j - c_j^\dagger\right)$ [39]:

$$\begin{aligned}
H = &-J\sum_i \left(a_{2i-1}a_{2i}a_{2i+1}a_{2i+2} + ia_{2i-1}a_{2i+2}\right)\\
&+ iJ_z\sum_i a_{2i}a_{2i+1}. \qquad (5)
\end{aligned}$$

In this basis, the XY (Ising) phase is mapped to a gapless (topological) phase, and the quantum phase transition becomes a topological transition. The topological phase is characterized by two Majorana zero-modes localized at the two ends of the chain. These topological Majorana modes can be seen by looking at the $J_z \gg J$ limit, where Eq. 5 converges to the Kitaev chain [39]. In this limit, edge Majorana fermions $a_1 = \gamma_1$ and $a_{2N} = \gamma_2$ are loosely connected to the rest of the chain and hence cause zero-energy modes in the spectrum. The zero-energy Majorana modes remain topologically protected, regardless of perturbations or interactions, for the entire topological phase. The existence of two Majorana modes at the two ends of the chain (γ_1 and γ_2) indicates that a zero-energy non-local fermion $d = \frac{\gamma_1 + i\gamma_2}{\sqrt{2}}$ can be defined. Because of its zero-energy nature, for an eigenstate of the Hamiltonian $|\psi_0\rangle$, another degenerate state $|\psi_1\rangle = d\,|\psi_0\rangle$ must exist with an opposite fermion parity. Therefore, the edge modes are responsible of the degenerate subspaces forming not only in the ground state, but throughout the entire spectrum [23, 39].

As a result, if we use the Majorana basis and choose the control parameters such that the system is in a topological phase at $T = 0$ (i.e. one topological zero-energy Majorana mode at each end), the OTOC with edge operators at $\beta = 0$ is always large (close to unity, Fig. 1) given the same control parameters. Whereas $\beta = 0$ edge OTOC remains small (close to 0 or -1 depending on the model) in the topologically trivial phase (i.e. no zero-energy Majorana modes at the ends). This observation, along with the robustness of the edge feature, suggests that the Majorana zero-energy modes localized at the edges are the origin of non-zero infinite-temperature edge OTOCs: infinite-temperature OTOCs with edge operators detect $T = 0$ phase transition via detecting the presence or absence of the edge Majorana zero-modes that are associated with the quantum phases at $T = 0$. This, in the end, leads the way to non-decaying infinite-temperature OTOCs and hence non-scrambling systems even when the Hamiltonian is manifestly interacting and non-integrable.

In the next sections, we analytically and numerically show that this effect can be understood based on the topological degeneracy. For a conventional quantum phase transition based on a spontaneous symmetry breaking, the ordered phase has multiple degenerate ground states (two for Ising symmetry breaking), while the disordered phase in general expects one unique ground state. This difference in ground state degeneracy can be detected in zero-temperature OTOCs [19]. At infinite temperature however, the contributions from the entire energy spectrum need to be summed over, and thus the infinite temperature measurements including OTOCs are not expected to be sensitive to the ground state features, e.g. ground state degeneracy and quantum phase transitions associated with it. However, certain TPTs have a totally different scenario, e.g. the topological phase of a Majorana chain, as explained above. The two-fold degeneracies that arise for the entire energy spectrum (in contrast to a conventional phase transition where degeneracy only arises in the ground state in general), causes the infinite-temperature OTOC to be sensitive to the zero-temperature physics.

We make use of the *dynamical decomposition method* to decompose the OTOC into topological and non-topological parts when the edge modes exist. This method was shown to be useful in proving the connection between OTOCs and symmetry-breaking phase transitions [19]. We will show that this method also provides us a direct and easy-to-calculate tool to determine if a system possesses topological order and the transition boundary between topologically non-trivial and trivial phases.

B. Dynamical decomposition method

The idea behind the method is to decompose the time-average of a dynamical quantity in mutually exclusive parts that reflect different physics by either being the leading order term or the corrections in the dynamical quantity via some assumptions [19]. For example, in Ref. [19] the assumptions are stated accordingly so that the decomposition reveals the ground state physics being the leading order term to the OTOC saturation value. Therefore, we could gain insight about the relation between scrambling and symmetry-breaking phase transitions via determining how and when the OTOC could be used to dynamically detect the quantum phases. In this sense, the method helps us to see what physics is at play in a complicated dynamical correlation function, e.g. OTOC. Now we are going to provide another example of the dynamical decomposition method: topological contribution being the leading order term in the (infinite temperature) OTOC saturation.

According to the dynamical decomposition, each correlator can be reduced to a combination of two basic constituents: eigenstate expectation values (EEV) that is the operator in the eigenbasis and the eigenstate occupation numbers (EON) that is the projection of initial state on the spectrum [40–42]. While in its most general format, the method requires the exact eigenstates and hence is numerically limited to exact diagonalization computations, the method can prove useful to derive analytical expressions for OTOCs when eigenstates have closed forms, e.g. via Bethe ansatz. We write the dynamic equation for the degenerate spectrum as,

$$\begin{aligned} F(t) = \sum_{\theta,\theta',\phi,\phi',\kappa} \sum_{\alpha,\beta,\gamma,\gamma',\tau} & c^*_{[\theta,\alpha]} c_{[\theta',\beta]} \\ & \times \exp\left[-i(E_{[\kappa,\tau]} - E_{[\theta,\alpha]} + E_{[\phi,\gamma]} - E_{[\phi',\gamma']})t\right] \\ & \times W^\dagger_{[\theta,\alpha][\phi,\gamma]} V^\dagger_{[\phi,\gamma][\phi',\gamma']} W_{[\phi',\gamma'][\kappa,\tau]} V_{[\kappa,\tau][\theta',\beta]}. \end{aligned} \tag{6}$$

The initial state is $|\psi(0)\rangle = \sum_{\theta,\alpha} c_{[\theta,\alpha]} \left|\psi_{[\theta,\alpha]}\right\rangle$, with eigenstates $\left|\psi_{[\theta,\alpha]}\right\rangle$ where the symbols represent degenerate manifold θ and the state α within, respec-

tively. Both the long-time saturation value and time-average of Eq. 6 could be obtained under the constraint $E_{[\tau,\kappa]} - E_{[\theta,\alpha]} + E_{[\phi,\gamma]} - E_{[\phi',\gamma']} = 0$. If we focus on an infinite-temperature initial state, $[\theta,\alpha] = [\theta',\beta]$ because $\mathbb{I} = |\psi_0\rangle\langle\psi_0| = \sum_{\theta,\alpha} |c_{[\theta,\alpha]}|^2 \left|\psi_{[\theta,\alpha]}\right\rangle\left\langle\psi_{[\theta,\alpha]}\right|$ and $|c_{[\theta,\alpha]}|^2 = \frac{1}{M}$. In order to simplify the expression further, we assume hermitian operators and $W = V$ since we focus on detecting the order and phase transitions. Then the saturation value is,

$$F_\infty = \sum_{\alpha\gamma\gamma'\tau} \left(\frac{2}{M} \sum_{\theta\phi} W_{[\theta,\alpha][\phi,\gamma]} W_{[\phi,\gamma][\phi,\gamma']} W_{[\phi,\gamma'][\theta,\tau]} W_{[\theta,\tau][\theta,\alpha]} - \frac{1}{M} \sum_{\theta} W_{[\theta,\alpha][\theta,\gamma]} W_{[\theta,\gamma][\theta,\gamma']} W_{[\theta,\gamma'][\theta,\tau]} W_{[\theta,\tau][\theta,\alpha]} \right) + \sum_{\alpha\gamma\gamma'\tau} \sum_{\theta\neq\phi\neq\phi'\neq\kappa} \frac{1}{M} W_{[\theta,\alpha][\phi,\gamma]} W_{[\phi,\gamma][\phi',\gamma']} W_{[\phi',\gamma'][\kappa,\tau]} W_{[\kappa,\tau][\theta,\alpha]}. \tag{7}$$

Alongside the assumption on the initial state, (i) infinite-temperature OTOC, we choose (ii) the ansatz on the matrix elements of the operator as $|W_{[\theta,\alpha][\theta',\beta]}|^2 \ll 1$ where $\theta \neq \theta'$ for the entire spectrum. This operator ansatz is more strict than the one used in Ref. [19] whose operator ansatz exerted an assumption only on the eigenstate where the phase transition is expected to happen. So, the relaxation in the initial state condition comes at a cost of making the operator condition tighter, reflecting an interesting trade-off between our two conditions. Later we will further elaborate on the necessity of the initial state assumption.

Under the assumptions (i)-(ii), the OTOC saturation dynamically decomposes into a topological leading order term F_{tp}^{∞} and non-topological corrections. In the topologically non-trivial phase, due to the degeneracies throughout the spectrum caused by the zero-energy modes, the fluctuations are suppressed between the matrix elements in all subspaces, implying $|W_{[\theta,\alpha][\theta,\beta]}| \sim \mathcal{O}(1)$. Hence the operator ansatz in the topologically non-trivial phase takes the form $|W_{[\theta,\gamma][\theta,\gamma']}|^2 \gg |W_{[\theta,\alpha][\theta',\beta]}|^2$. Therefore, we derive the leading order term in this phase as,

$$F_{tp}^{\infty} = \frac{1}{M} \sum_{\theta} \sum_{\alpha\gamma\gamma'\tau} W_{[\theta,\alpha][\theta,\gamma]} W_{[\theta,\gamma][\theta,\gamma']} W_{[\theta,\gamma'][\theta,\tau]} W_{[\theta,\tau][\theta,\alpha]}. \tag{8}$$

The operator ansatz in the topologically non-trivial phase simultaneously guarantees that the OTOC Eq. 7 is dominated by the topological contribution Eq. (8). Similar to a disordered phase in a symmetry-breaking phase transition, in the topologically trivial phase the fluctuations are expected to exist between the matrix elements in any subspace, leading to the absence of order $|W_{[\theta,\alpha][\theta,\beta]}| \sim 0$, and hence $F_{tp}^{\infty} \sim 0$. Then the non-topological correction term dominates the OTOC, while the operator ansatz $|W_{[\theta,\alpha][\theta',\beta]}|^2 \ll 1$ still guarantees bounded non-topological correction term. As we will detail in the following sections, this is almost always the case in non-integrable systems, since the operator ansatz is a looser version of a Eigenstate Thermalization Hypothesis (ETH) criteria: $|W_{\theta\theta}| \gg |W_{\theta\theta'}|$ for a non-degenerate spectrum, implying that the off-diagonal elements are suppressed compared to the diagonal elements [42]. For a degenerate spectra where the topological order can form, the dynamical decomposition of OTOC into topological and non-topological contributions provides a similar condition to the second criteria of ETH [42–44]. Then, as it could be anticipated, the integrable systems do not necessarily have a bounded non-topological correction term, given that the ETH criteria are generally violated for these systems [42–44]. Hence we predict that the topological order could be concealed by the integrability in integrable systems. To conclude, since (i) Eq. (8) captures the degenerate subspace contributions throughout the spectrum and (ii) when the corrections remain bounded, the topological order and hence a TPT should be dynamically detectable via OTOC saturation value of an operator that satisfies the operator ansatze in topologically trivial and non-trivial phases at infinite-temperature.

C. Transverse-field Ising Model

Here we use an exactly solvable model to demonstrate the role of topology in the OTOC. The Hamiltonian for the transverse-field Ising model with open boundary conditions is,

$$H = -J \sum_{j=1}^{N-1} \sigma_j^z \sigma_{j+1}^z + h \sum_{j=1}^{N} \sigma_j^x. \tag{9}$$

Let us first take a look at the OTOC saturation value derived from the real-time dynamics at $\beta = 0$. When we set the OTOC operators to one of the edge spin operators in z-direction, σ_1^z, we obtain the lines with green-circles and light-blue diamonds for $N = 14$ and $N = 50$, respectively in Fig. 2a. The simulation with $N = 50$ spins is performed with matrix product states (MPS), (see Appendix A for details). Here the error bars stand for the extend of oscillations in time, as we time-average the real part of the OTOC signal in a time interval of $t = \frac{\pi}{4}10 \sim 7.85$ [1/J]. We observe that the curve steadily diverges from

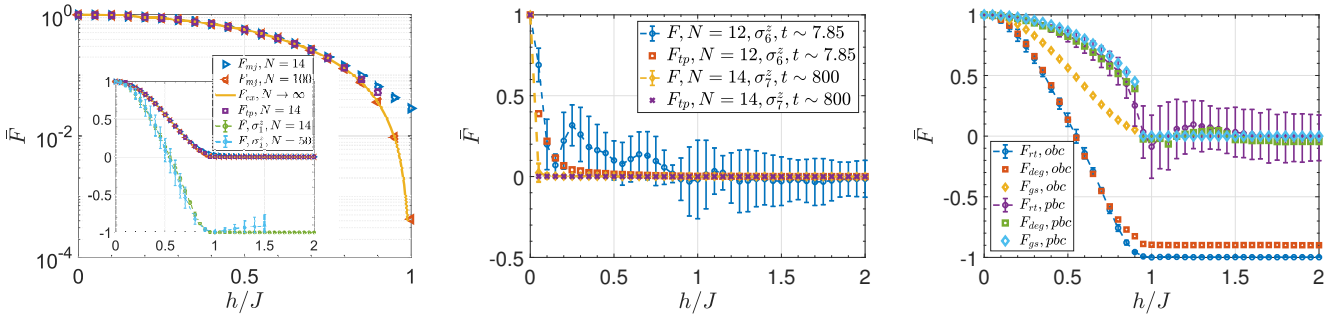

(a) (b) (c)

FIG. 2. Transverse-field Ising model results. (a) The OTOC saturation values of the edge spin operators σ_1^z, calculated via the topological OTOC Eq. 8 at $N = 14$ (purple-circles); for BdG Hamiltonian with Majorana edge modes at $N = 14$ (blue right-pointing triangles) and $N = 100$ (red left-pointing triangles); exact form derived from the two-point correlators (solid-orange) both in logarithmic and linear scales (inset); the real-time OTOC dynamics (green circles) at $N = 14$ and (light-blue diamonds) at $N = 50$ where we used MPS (see Appendix A) in the inset with linear scale. (b) The OTOC saturation values of the bulk spin operators σ_6^z at $N = 12$ for a time interval $t = \frac{\pi}{4}10 \sim 7.85$ [1/J] (blue circles: real-time dynamics, red-squares: the topological OTOC Eq. 8) and σ_7^z at $N = 14$ for a time interval $t = \frac{\pi}{4}10^3 \sim 800$ [1/J] (orange diamonds: real-time dynamics, purple crosses: the topological OTOC Eq. 8). (a)-(b): the initial state is set to $\beta = 0$ state. (c) The zero-temperature OTOC saturation values (initial state is set to the ground state) of σ_1^z operator with open boundary condition in a time interval $t \sim 7.85$ [1/J]: the real-time dynamics F_{rt} (blue-circles), the dynamical decomposition theory prediction F_{deg} (red-squares) and the ground-state manifold contribution in this result F_{gs} (orange-diamonds) (App. A); contrasted with periodic boundary conditions of σ_7^z operator in a time interval $t \sim 20$ [1/J]: F_{rt} (purple-circles), F_{deg} (green-squares) and F_{gs} (light blue-diamonds). All curves in (c) are at $N = 14$.

unity to $F_\infty \sim -1$ when $h < 1$ [J] and stays at $F_\infty \sim -1$ at $h > 1$ [J], hence marking the point $h \sim 1$ [J] as a transition point. On the contrary, when we choose a bulk spin operator, σ_6^z, this feature disappears (blue-circles at $N = 12$ and orange-diamonds at $N = 14$ in Fig. 2b). The line with blue-circles in Fig. 2b demonstrates a drop in the saturation value well before the transition point when time is short enough $t \sim 7.85$ [1/J]. While increasing the size (to $N = 14$) and the time interval of averaging (to $t \sim 800$ [1/J]) results in even steeper decline to zero and a steady $F_\infty = 0$ value for any higher magnetic field h. This observation clearly reflects that the physics captured by edge- and bulk-spin operators are different; curiously enough a similar observation to what we presented for the XXZ model earlier. To further show how the real-time OTOC dynamics look like, we contrast the curves belonging to σ_1^z operator (blue-solid and orange-dotted for $h = 0.1$ and $h = 0.9$, respectively) with the curves of σ_6^z (red-dashed and purple-dotted dashed for $h = 0.1$ and $h = 0.9$, respectively) for a chain of $N = 12$ in Fig. 3. Notice how the order in time-average (or the saturation value) of the signal is captured when an edge operator is utilized, whereas a bulk operator results in a decay for smaller h and a damped-oscillatory behavior around zero for larger h values. Now let us explain these different behaviors of OTOC.

Eq. 9 can be rewritten in Majorana fermion representation with no interactions between Majorana fermions,

$$H = -iJ \sum_{j=1}^{N-1} a_{2j} a_{2j+1} - ih \sum_{j=1}^{N} a_{2j-1} a_{2j}, \qquad (10)$$

where we used Eqs. 4. When the field h is set to zero, the edge operators a_1 and a_{2N} remain unpaired and hence totally localized at the edges. Turning on the field lets the localized Majorana modes exponentially decay into the chain. Let us first show what the doubly-degenerate spectrum in Eq. 10 corresponds to in Ising model Eq. 9. The non-local fermion operator d could also be written as,

$$d = \frac{\gamma_1 + i\gamma_2}{\sqrt{2}} = \frac{1}{\sqrt{2}} \left[\left(c_1 + c_1^\dagger \right) + \left(c_N - c_N^\dagger \right) \right]$$
$$= \frac{1}{\sqrt{2}} \left(-\sigma_1^z + i \prod_{j<N} \sigma_j^x \sigma_N^y \right), \qquad (11)$$

where we used Eqs. 4 in the second line. Note that the operator Eq. 11 forms degenerate subspaces spanned by the states that are dictated by Ising symmetry Z_2, e.g. $|\psi_0\rangle = \frac{1}{\sqrt{2}} \left(|\uparrow\rangle^{\otimes N} + |\downarrow\rangle^{\otimes N} \right)$ and $|\psi_1\rangle = \frac{1}{\sqrt{2}} \left(|\uparrow\rangle^{\otimes N} - |\downarrow\rangle^{\otimes N} \right)$ for the ground state manifold.

We construct the Bogoliubov-deGennes (BdG) matrix for Eq. 10 and obtain the zero modes to calculate Eq. 8 in a doubly-degenerate spectrum. The main quantity to calculate is $W_{[\theta,\alpha][\theta,\gamma]} = \langle \psi_{[\theta,\alpha]} | W | \psi_{[\theta,\gamma]} \rangle$ where $|\psi_{[\theta,\gamma]}\rangle$ and $|\psi_{[\theta,\alpha]}\rangle$ are even and odd parity states in a doubly-degenerate subspace. Then $|\psi_{[\theta,\gamma]}\rangle = d |\psi_{[\theta,\alpha]}\rangle = f(h) \left(\frac{\gamma_1 + i\gamma_2}{\sqrt{2}} \right) |\psi_{[\theta,\alpha]}\rangle$, where $f(h)$ is a function of magnetic field h and $f(h = 0) = 1/\sqrt{2}$, however decreases as $h \to 1$ ($h = 1$ is the critical point in Eq.

9). The quantity that we need to calculate becomes $\langle\psi_{[\theta,\alpha]}| W f(h) (\gamma_1 + i\gamma_2) |\psi_{[\theta,\alpha]}\rangle / \sqrt{2}$. We expect the effect to appear when we use edge spins, hence

$$W = \sigma_1^z = \left(c_1 + c_1^\dagger\right) = \gamma_1 \tag{12}$$

$$W = \sigma_N^z = \prod_{j<N} \left(1 - 2c_j^\dagger c_j\right) \left(c_N + c_N^\dagger\right)$$

$$= \mathbb{P} \left(c_N - c_N^\dagger\right) = i\mathbb{P}\gamma_2, \tag{13}$$

where $\mathbb{P} = \prod_j^N \left(1 - 2c_j^\dagger c_j\right)$ is the parity operator. Eqs. 12-13 show the operator W in Ising, Dirac and Majorana bases, respectively. If we work with the operator Eq. 12,

$$\langle\psi_{[\theta,\alpha]}| f(h)\gamma_1 \left(\frac{\gamma_1 + i\gamma_2}{\sqrt{2}}\right) |\psi_{[\theta,\alpha]}\rangle = \frac{2f(h)}{\sqrt{2}}, \tag{14}$$

where we utilized $(\gamma_i)^2 = \mathbb{I}$ and $-i\gamma_1\gamma_2 |\psi_{[\theta,\alpha]}\rangle = -|\psi_{[\theta,\alpha]}\rangle$ since $|\psi_{[\theta,\alpha]}\rangle$ is an odd-parity state. Similarly for Eq. 13,

$$if(h) \langle\psi_{[\theta,\alpha]}| \mathbb{P}\gamma_2 \left(\frac{\gamma_1 + i\gamma_2}{\sqrt{2}}\right) |\psi_{[\theta,\alpha]}\rangle = \frac{2f(h)}{\sqrt{2}}, \tag{15}$$

where we additionally use $\mathbb{P}|\psi_{[\theta,\alpha]}\rangle = -|\psi_{[\theta,\alpha]}\rangle$. At $h = 0$, $W_{[\theta,\alpha][\theta,\gamma]} = 1$ for each θ and α. Thus Eq. 8 reads $F_{tp}^\infty = 1$, successfully showing that there is no scrambling at this limit. For general $f(h)$ which we calculate with numerics, we obtain $F_{tp}^\infty = |W_{[\theta,\alpha][\theta,\gamma]}|^4 = f(h)^4/4$. The lines with blue right-pointing triangles and red left-pointing triangles in Fig. 2a show this result calculated with Majorana edge modes of BdG Hamiltonian at sizes of $N = 14$ and $N = 100$ sites, respectively. These curves should be compared with the degenerate subspace contributions in OTOC F_{tp}^∞, Eq. 8, calculated for the Ising chain at $N = 14$ in Fig. 2a (purple-squares). The curves at $N = 14$, F_{mj} and F_{tp}^∞ as well as $N = 100$ match well up to the transition point where finite-size effects show up. The difference between the curves F_{mj} of $N = 14$ and $N = 100$ at the transition point can be seen in the logarithmic scale of Fig. 2a as a demonstration of the finite-size effects. Therefore the OTOC clearly exhibits Majorana edge physics, encoded in the degenerate subspaces of the energy spectrum. We can further derive an analytical expression for this topological contribution to OTOC. Ref. [27] studies two-point correlators of edge Majorana fermions $C_1(t) = \langle\psi| W(t)W |\psi\rangle$ in its saturation regime and finds that this correlator is a direct indicator of the topological phase and the transition in the Kitaev chain (and hence the Ising chain). We apply the dynamical decomposition to this correlator and find that it saturates at,

$$C_\infty = \frac{1}{M} \sum_\theta \sum_{\alpha,\gamma} W_{[\theta,\alpha][\theta,\gamma]} W_{[\theta,\gamma][\theta,\alpha]}, \tag{16}$$

in the ordered phase for a $\beta = 0$ initial state. Therefore, we see that a two-point correlator will always reduce to Majorana edge physics at the infinite-temperature with

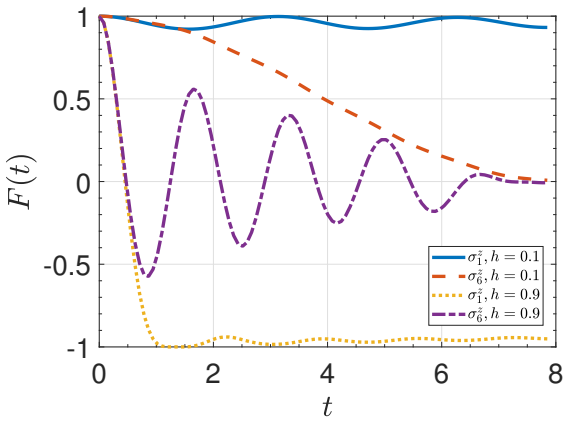

FIG. 3. The OTOC dynamics $F(t)$ with respect to time for transverse-field Ising model with open-boundary conditions when the initial state is an infinite-temperature state. The blue-solid and the orange-dotted lines are the OTOC of edge σ_1^z operator for $h = 0.1$ and $h = 0.9$, respectively. The red-dashed and the purple-dotted dashed lines are the OTOC of edge σ_6^z operator for $h = 0.1$ and $h = 0.9$, respectively. The OTOC dynamics of edge and bulk operators demonstrate different physics.

no conditions on the operator W. Ref. [27] provides a simple functional form of Eq. 16: $C_\infty = 1 - h^2$ for $h < J$ and $C_\infty = 0$ for $h > J$. We substitute this analytical result into Eq. 16 and obtain $W_{[\theta,\gamma][\theta,\alpha]} = \sqrt{1 - h^2}$ for $h > J$ in the topologically non-trivial phase. Therefore, we straightforwardly calculate the topological contribution to OTOC in its time-average: $F_{tp}^\infty = \left(1 - h^2\right)^2$. The solid-orange line in Fig. 2a is the exact result, matching perfectly with our other calculations until the phase transition point, where it continues to match with F_{mj} calculation at $N = 100$. Hence, we see that our Ising model calculations of topological contribution to OTOC suffers from the finite-size effects at the phase boundary.

Having demonstrated the point (i) that is the OTOC captures the order in topologically non-trivial phases verifying the Eq. (8), we study the point (ii) in detail: does non-topological correction remain bounded and hence, can we accurately mark the TPT point? We observe that OTOC Eq. 7 reduces to the topological leading order term (Eq. 8) only when $h \lesssim 0.2$ (green-circles and purple-squares in Fig. 2a). Starting from $h \sim 0.2$ [J], as we increase the field strength, non-topological correction starts to increase and eventually dominates the OTOC saturation. Exactly where the topological contribution approaches to 0 and hence pointing to the TPT that is about to happen, the OTOC itself, approaches to $F_\infty \sim -1$. To understand the relation between this behavior and the integrability of the system, we plot the matrix elements $|V_{\beta\alpha}|^2$ for various β in the spectrum at different h values in Fig. 4. The first four subfigures (a)-(d) are for an edge spin operator σ_1^z, whereas the rest (e)-(h) are for a bulk spin operator. Deep in the

topologically non-trivial phase, $h = 0.1$, we see that the operator ansatz is satisfied $|V_{[\theta,\gamma][\theta,\gamma']}|^2 \gg |V_{[\theta,\gamma][\theta',\gamma']}|^2$ for an edge spin (blue-circles). For a bulk spin, the operator ansatz is valid only in the ground state subspace, hence it is actually $|V_{[1,\gamma][1,\gamma']}|^2 \gg |V_{[1,\gamma][\theta',\gamma']}|^2$, the condition put forward by Ref. [19] for the dynamical detection of symmetry-breaking phase transitions via OTOCs. This is how the edge spins preserve the topological order in the OTOC throughout the spectrum, while the bulk spins can preserve only the symmetry-breaking order. Closer to the transition point, $h = 0.8$, the order $|V_{[\theta,\gamma][\theta,\gamma']}|^2$, expectantly, decreases while the off-diagonal matrix elements $|V_{[\theta,\gamma][\theta',\gamma']}|^2$ grow, which is a signature of integrability. Eventually the operator ansatz in the topologically non-trivial phase starts to break down, hence explaining how the OTOC saturation starts to be dominated by an integrability effect over the topological contribution. Note that this breakdown in the operator ansatz does not happen in the bulk spin at a ground state, Fig. 4e. The red-squares at $h = 0.8$ exhibit $|V_{[1,\gamma][1,\gamma']}|^2 \gg |V_{[1,\gamma][\theta',\gamma']}|^2$, though clearly getting weaker as we approach the transition point. To demonstrate how the operator dynamics reflect itself in the OTOC saturation value, we plot Fig. 2c where the purple-circles show the real-time OTOC dynamics and the green-squares are the theory predictions for zero-temperature OTOC (when the initial state is set to the ground state). The blue-diamonds are the leading-order term which is the ground state subspace contribution to the saturation value. The OTOC saturation captures the symmetry-breaking phase transition from ordered to disordered phases as originally shown in [20] and explained in [19].

In the topologically trivial phase, $h = 1.5$, the operator ansatz is still satisfied $|V_{[\theta,\gamma][\theta',\gamma']}|^2 \ll 1$, though being borderline: $|V_{[\theta,\gamma][\theta',\gamma']}|^2 \sim 0.1$. This could be seen in orange-diamonds in Figs. 4a-4d. However more importantly, we realize only a certain number of off-diagonal matrix elements are non-zero and the rest is zero up to machine precision in Figs. 4a-4d. Additionally, the number of non-zero off-diagonal matrix elements match with the system size, meaning that there are 12 nonzero matrix elements in $N = 12$ and etc., as seen in Fig. 5a at different system sizes for a ground state. Even though the operator ansatz is still borderline for a bulk spin in a ground state, Fig. 4e, by no means these matrix elements are the only non-zero ones where we observe a scattering rather than a clear arc pattern of matrix elements of Figs. 4a-4d. We relate this unusual order in the off-diagonal matrix elements of an edge spin in an integrable system to the 'integrability order'. This effect seems to dominate the topologically trivial phase by letting us observe that the OTOC saturation value Eq. 7 always converges to $F_\infty \sim -1$ regardless of the interval of time-averaging which implies that the temporal dephasing does not occur, consistent with integrable systems. The same effect also causes the breakdown of the operator ansatz while approaching the TPT point, previously discussed (red-squares in Figs. 4a-4d possess the same arc pattern). Hence the topological order in Fig. 2a is increasingly shadowed by an 'integrability' order as h increases.

Now interestingly we also observe that the integrability order is independent of the initial state. Even the operator ansatz for the detection of symmetry-breaking phase transitions is violated, when an edge spin is chosen (Fig. 4a) as seen in Fig. 2c. The theory prediction (red-squares) and the ground state subspace contribution (orange-diamonds) start to mismatch deep in the ordered phase, $h \geq 0.2$. Therefore, the OTOC does not reduce to the ground state physics for an edge spin even for zero-temperature, meaning the OTOC cannot dynamically detect the ordered and disordered phases. Instead, it detects the integrability order that build up as h increases. We note that this is the case in any eigenstate for an edge-spin: Fig. 5b compares the off-diagonal matrix elements $|W_{\beta\alpha}|^2$ for a variety of β. Note how these matrix elements possess an order with the same strengths. This is the underlying reason why an infinite temperature and zero temperature OTOC of edge spins could give the same saturation behavior seen in Figs. 2a and 2c.

In conclusion for the section, the OTOC saturation value of an edge operator and hence the information scrambling, when edge modes exist, can capture the topological order at infinite temperature up to non-topological corrections depending on the model. This connection that we probe further encourages us to explore the interplay between topological order and scrambling in interacting and non-integrable systems, since the integrability order could outcast the topological order.

III. THE INTERPLAY BETWEEN TOPOLOGICAL ORDER AND SCRAMBLING

Could we find a model whose OTOC saturation regime encodes mostly and preferably only the topological physics? In other words, is there a model where a local operator at the edge of the system perfectly satisfies the operator ansatz, so that the corrections to the OTOC remain bounded for any field h? Having observed that the integrability shadows the topological contribution to OTOC in the integrable Ising model, we propose to break the integrability and study a non-integrable version of Ising model,

$$H = -J\sum_{j=1}^{N-1}\sigma_j^z\sigma_{j+1}^z - \Delta\sum_{j=1}^{N-2}\sigma_j^z\sigma_{j+2}^z + h\sum_{j=1}^{N}\sigma_j^x, \quad (17)$$

$$= -iJ\sum_{j=1}^{N-1}a_{2j}a_{2j+1} + \Delta\sum_{j=1}^{N-2}a_{2i}a_{2i+1}a_{2i+2}a_{2i+3}$$

$$- ih\sum_{j=1}^{N}a_{2j-1}a_{2j}, \quad (18)$$

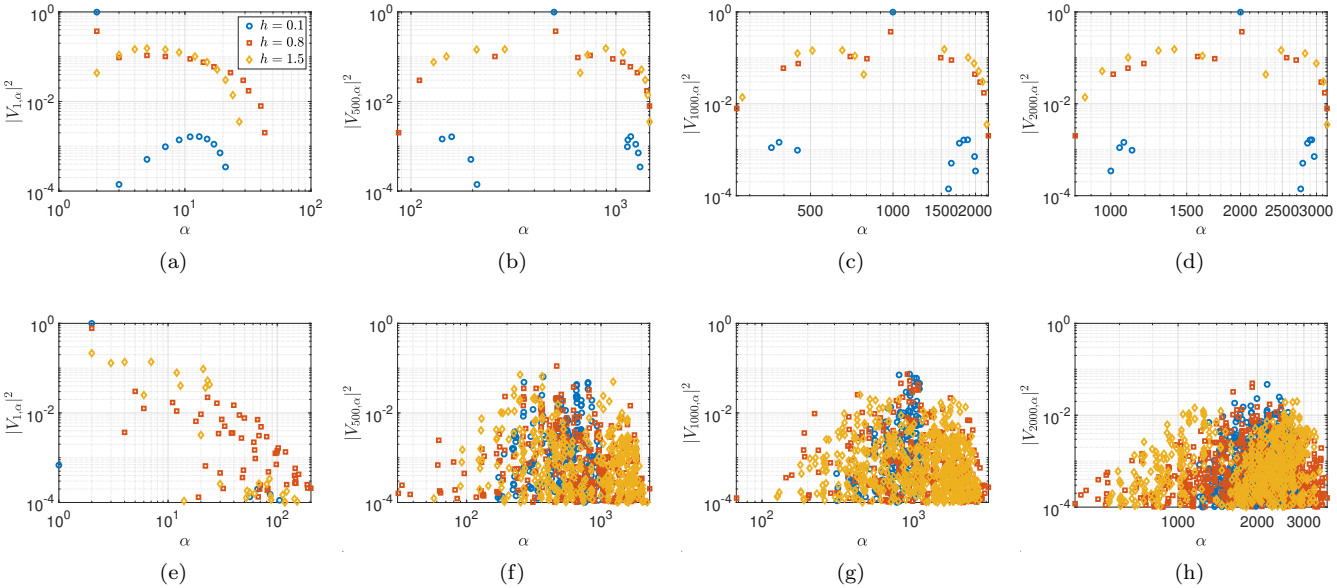

FIG. 4. The operator ansatz tested on Ising model. Matrix elements $|V_{\beta\alpha}|^2$ are plotted for $\beta = 1$ (a), $\beta = 500$ (b), $\beta = 1000$ (c) and $\beta = 2000$ (d) with respect to α for an edge operator σ_1^z (open boundary); same β (e)-(h) for a bulk operator (periodic boundary) at a size $N = 12$. Blue-circles, red-squares and orange-diamonds stand for field strength $h = 0.1$ [J], $h = 0.8$ [J] and $h = 1.5$ [J], respectively for all subfigures.

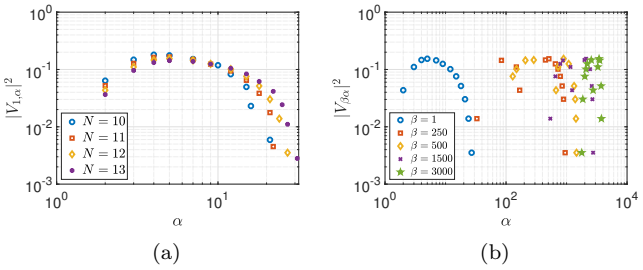

FIG. 5. The non-zero off-diagonal elements of an edge spin $|W_{\beta\alpha}|^2$ (a) for $\beta = 1$ ground state for various system sizes $N = 10$ (blue-circles), $N = 11$ (red-squares), $N = 12$ (orange-diamonds) and $N = 13$ (purple-dots); (b) for various $\beta = 1$ (blue-circles), $\beta = 250$ (red-squares), $\beta = 500$ (orange-diamonds), $\beta = 1500$ (purple-asterisks) and $\beta = 3000$ (green-pentagons).

where Δ is the next-nearest neighbor coupling between spins in Eq. 17 and breaks the integrability of the model. The strength Δ introduces interactions between Majorana fermions in Eq. 18.

We study the OTOC saturation value for long times, e.g. $t \sim 800$ [1/J] to guarantee the temporal dephasing. Fig. 6a shows the OTOC saturation values of real-time dynamics when the operator is set to edge-spin σ_1^z for sizes $N = 12$ (orange-circles) and $N = 14$ (purple-squares). The quantum phase transition point is $h_c = 1.14$ [J] for weak interactions $\Delta = 0.1$, as denoted by the black line. We see the effect of finite size as the dip signature shifts towards the phase transition point with the increasing system size N. The topological contribution, F_{tp}^{∞} can also be seen in Fig. 6a at the blue pentagrams and red-diamonds. As we increase the system size, the data shows a shift to the right towards the phase transition point, as well as an increase in the topological contribution. We plot the topological contribution of system sizes ranging from $N = 10$ to $N = 15$ in logarithmic scale in Fig. 6c. Note that the decrease in the logarithmic scale reveals that F_{tp} continues to decrease in h as a power-law when $F_{tp} \lesssim 0.1$, approaching to the phase transition point. This steeper decline to zero that is visible only in logarithmic scale, is a sign of disappearing degeneracies in the spectrum as h increases, and hence a sign of finite-size effects. Additionally, given that we introduce cut-offs in the computations of sums in the theory Eqs. (7)-(8) for efficient computation (see App. A), the data in F_{tp} are slightly underestimated. Therefore F_{tp} in Figs. 6 are a lower bound to the exact values without a cut-off. The power-law decrease in F_{tp} demonstrates regularly increasing slope for the topological contribution to OTOC in h as N increases. The parameters read $b = -34.75$, $b = -38.4$, $b = -42.39$, $b = -43.71$, $b = -45.63$ and $b = -50.7$ for $N = 10$ to $N = 15$, respectively in fitting $F_{tp} \propto ah^b$ where a is a constant. Hence we expect that in thermodynamic limit, the topological contribution of non-integrable model with weak integrability breaking gives a similar trend to the topological contribution of the integrable model, Fig. 2a. On the contrary, the OTOC saturation of a bulk spin in Fig. 6b behaves drastically different: as we increase the

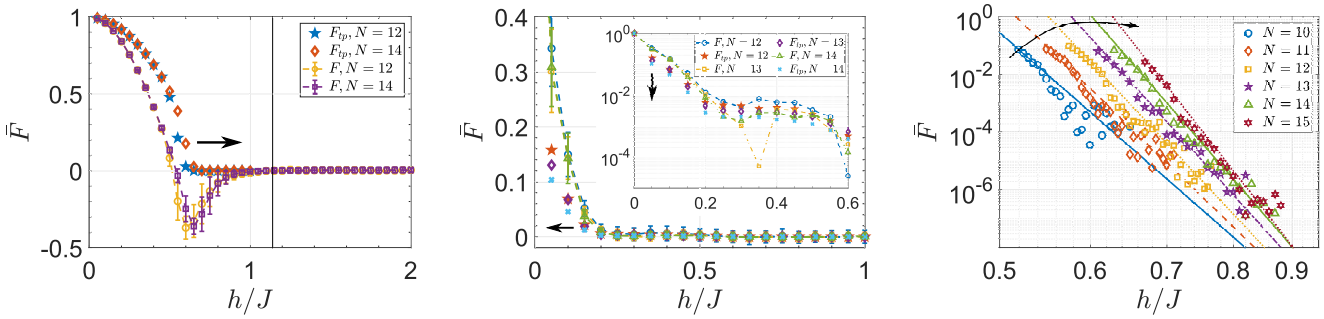

(a) (b) (c)

FIG. 6. Non-integrable transverse-field Ising model results of small integrability breaking term $\Delta = 0.1$ [J]. The OTOC saturation values of a Hamiltonian with (a) an edge spin in linear scale, (b) a bulk spin in linear and logarithmic (inset) scale and (c) an edge spin in logarithmic scale. In (a) blue pentagrams and red diamonds show the topological OTOC, F_{tp} whereas the orange circles and purple squares show the OTOC saturation value, F_∞ at $N = 12$ and $N = 14$ system sizes, respectively. Black line shows the TPT point, $h_c \sim 1.14$ [J]. (b) Red pentagrams, purple diamonds and light-blue crosses show F_{tp} whereas the blue circles, orange squares and green triangles show F_∞ for $N = 12$, $N = 13$ and $N = 14$, respectively for a bulk spin. (c) The topological OTOC F_{tp} of an edge spin for system sizes ranging from $N = 10$ to $N = 15$ (blue-circles, red-diamonds, orange-squares, purple-pentagrams, green-triangles and bordeaux-hexagrams, respectively). All curves have open boundary conditions and a time interval of $t \sim 800$ [1/J].

system size, both F_∞ and F_{tp} approach to zero for all h, and hence gets even farther away from the transition point.

In conclusion, via breaking the integrability weakly OTOC saturates to a value mostly dictated by its topological contribution. Increasing the interaction strength to $\Delta = 0.5$ [J] lets even more clear match happen between F_∞ and F_{tp}^∞ in Fig. 7a for both the edge spin (blue-circles F_∞ and red-pentagrams F_{tp}) and a bulk spin (orange-squares F_∞ and purple-diamonds F_{tp}). Fig. 7b shows the OTOC saturation and its topological contribution for a bulk spin with increasing system size. We observe that the topological order decreases as the system size increases, pointing to vanishing order in thermodynamic limit for a bulk spin. Unlike in the case of weak integrability breaking, increasing the interactions destroys the topological order in the edge spins as well. Fig. 7c similarly demonstrates the saturation value and its topological contribution for different system sizes. The first observation is that F_{tp} approaches to the phase transition point, $h_c \sim 1.6$ that is denoted by the black line, as N increases. However, the topological order decreases as N increases. This observation is detailed in Figs. 8, where we focus on the interval $h < 1$ in logarithmic and linear scales. Hence, we conclude that increasing the interactions, expectantly, delocalizes the Majorana edge modes and the vanishing topological order is captured via the OTOCs. The effect of interactions is best observed when the scrambling decay trends of edge spin operators in Figs. 6a and 7a are compared. When the interactions are zero or weak, the decay has a polynomial form $(a - h^2)^2$, whereas as the interaction strength increases, the decay transforms into an exponential form $\sim a\exp(bh)$.

The OTOC saturation value indeed becomes an order parameter for the topologically non-trivial phase: even though this order parameter could be highly nonlocal in the Dirac fermion representation, it is local in spin description. Further, it is supposed to *stay local* for a weakly-interacting chain in thermodynamic limit based on the observation of increasing topological order with the system size (Fig. 6c). This observation tells us that the scrambling in the system is negligible when the topological order exists and hence the initially local operator σ_1^z continues to be local throughout the time-evolution. Therefore, we demonstrate how topologically-protected degrees of freedom fight against being scrambled, either completely preventing or restricting the operator spreading and thus exhibiting a clear interplay between the topological order and scrambling. An interacting and a non-integrable system, e.g. our model under study in this section, is always expected to scramble down to zero where the decay rate depends on the global conservation laws existing in the Hamiltonian. However, our results indicate that this does not always need to be the case and the scrambling can be severely hindered by the topological protection of the information spreading. In this context, our findings confirm our intuition and current understanding on the information scrambling in quantum many-body systems [45]. Further they imply that the topological protection might work against the scrambling not only due to the internal thermalizing dynamics of the system, but also the scrambling due to the detrimental effects of an environment [46, 47].

In conclusion for the section, the non-integrability provides a better reduction to topological contribution in OTOC saturation value via making sure that the operator at the edge sufficiently satisfies the operator ansatz. This renders the OTOC saturation value an or-

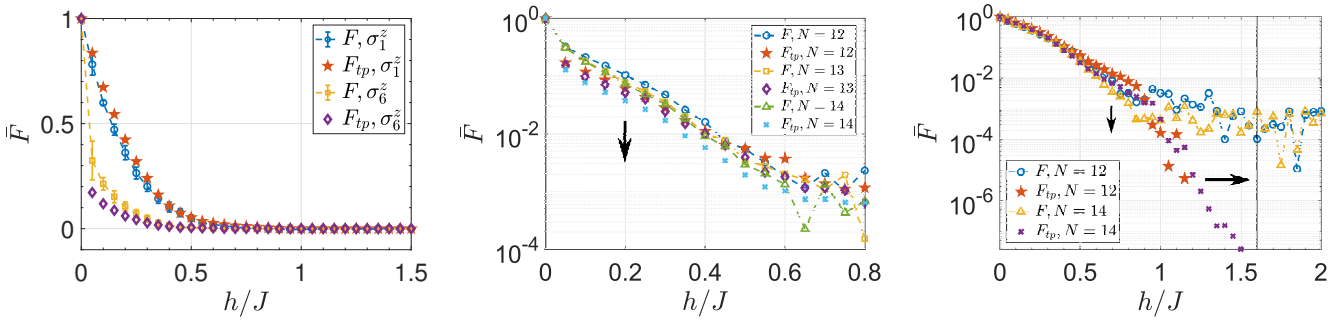

(a) (b) (c)

FIG. 7. Non-integrable transverse-field Ising model results of large-integrability breaking term $\Delta = 0.5$ [J]. (a) The OTOC saturation values of a Hamiltonian with an edge spin (blue-circles: F_∞, red-pentagrams: F_{tp}) and a bulk spin (orange-squares: F_∞, purple-diamonds: F_{tp}) at $N = 12$ system size. (b) A detailed look at the bulk spin shows a regular decrease as the system size increases. The OTOC saturation F_∞ and the topological contribution F_{tp} for $N = 12$ (blue-circles and red-pentagrams), $N = 13$ (orange-squares and purple-diamonds) and $N = 14$ (green-triangles and light-blue crosses). (c) Unlike in the case of small-integrability breaking, the OTOC saturation for edge spin also decreases with the system size: F_∞ and F_{tp} for $N = 12$ (blue-circles and red-pentagrams) and $N = 14$ (orange-triangles and purple crosses). Black line shows the TPT point, $h_c \sim 1.6$ [J]. All curves have open boundary conditions and a time interval of $t \sim 800$ [1/J].

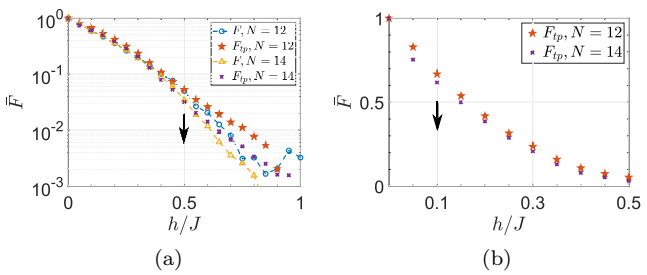

(a) (b)

FIG. 8. A detailed look at the OTOC saturation dynamics of an edge spin. (a) Fig. 7c focused at the interval of $0 < h < 1$ [J] to demonstrate the decline in both F_∞ and F_{tp} as the system size N increases. (b) The topological contribution F_{tp} of Fig. 7c is shown in linear scale to demonstrate the decline even in small h values.

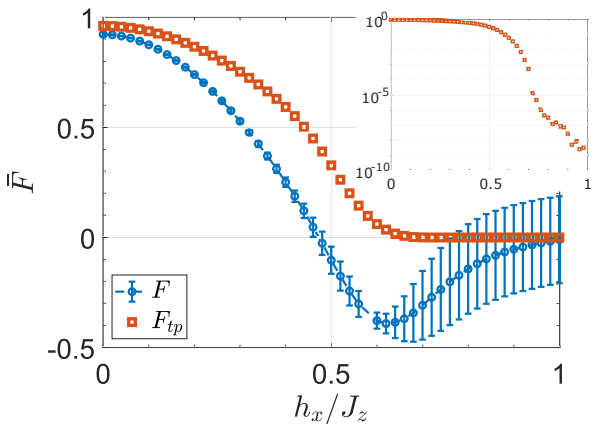

FIG. 9. The OTOC saturation values of real-time dynamics (blue-circles) and its topological contribution (red-squares) in the transverse-field XXZ-model with respect to h_x/J_z where $J_z = 10$ [J] and h_x is the strength of the transverse-field. The inset shows the topological contribution in logarithmic scale.

der parameter for the topological order. The OTOC of weakly interacting systems tend not to decay, a reflection of the preserved topological order in the system. On the contrary, strongly-interacting systems show information scrambling more in accordance with the strongly-interacting Majorana fermions.

A. The XXZ model revisited

Now we go back to our observation on XXZ model stated in the introduction and calculate F_{tp}^∞, the topological contribution Eq. 8. The lines with red-squares, purple-dots and light-blue right-pointing triangles plot F_{tp}^∞ for an edge-spin σ_1^z (obc), a bulk-spin σ_1^z (pbc) and a bulk-spin σ_7^z (obc) operators, respectively in Fig. 1. When the periodic boundary condition is set, the topological contribution is always zero regardless of the J_z coupling strength. The signal in OTOC with an edge spin operator that we presented earlier in the text has the major contribution from the degenerate-subspaces in the Ising phases. Even though this model has interactions in its Majorana representation Eq. 5, it is still an integrable system which explains why its OTOC saturation value does not completely match with its topological contribution in a long-time evolution. The edge modes in the XXZ model are always interacting due to the couplings in other axes, hence the signal is always $F_\infty < 1$, approaching to $F_\infty \sim 1$ at the limit of $J_z/J \gg 1$ where the edge modes are increasingly localized. The topo-

logical contribution in the XXZ model becomes zero in the XY-phase consistent with a gapless phase. As expected, when a bulk spin is chosen in open-boundary chain we still observe the effect of exponentially decaying edge modes towards the middle of the chain as a slight increase of F_{tp}^{∞} in the transition to Ising phases from XY-phase (right-looking triangles). To make our argument even stronger, we add a transverse-field to the Hamiltonian Eq. 2 and break the total spin conservation as well as the integrability of XXZ-chain. Fig. 9 shows the OTOC dynamics (blue-circles) and the topological contribution (red-squares) of an edge-spin operator with respect to the transverse-field strength h_x/J_z when $J_z = 10J$ is set for open-boundary condition. Notice how Fig. 9 is similar with the edge spin results of Fig. 6a, the non-integrable Ising model. This similarity is intuitive when we compare the Majorana representations of XXZ- and non-integrable Ising models, Eqs. 5-18. The integrability-breaking term with Δ strength in Eq. 18 corresponds to the couplings in X- and Y-axes with J strength in Eq. 5; both introducing interactions between Majorana fermions. When we additionally add h_x to the XXZ model and see if there is a transition occurring in h_x, we reproduce the OTOC of non-integrable Ising model and hence observe a TPT in the transverse-field XXZ-model. We further note that without a transverse-field, the XXZ model has an OTOC that mostly reduces to its topological contribution even though it is an integrable model. In this sense, the XXZ model has a more clear dynamical signature of the topological order than the integrable Ising model, which is shadowed by the integrability order.

IV. ROBUSTNESS OF THE TOPOLOGICAL ORDER AGAINST SCRAMBLING

In the final section of our paper, we focus on how robust the relation between scrambling and the topological order is. We study this question in two different pathways: i) How does the temperature affect our results? ii) Could OTOC capture the topological order when the boundary conditions are different?

A. Topological order in finite-temperature OTOC

We study if the topological order can be detected at finite-temperatures where we set the model to weakly-interacting non-integrable Ising model, $\Delta = 0.1$ [J]. We observe that the trend captured for the infinite temperature OTOC persists for finite temperatures in Fig. 10 for $T = 5$ [J] and $T = 1$ [J]. The finite-size scaling in F_{tp} suggests that the TPT point can be marked in the thermodynamic limit at any temperature. Hence the interplay between the information scrambling and the topological order is not limited to infinite-temperature OTOC, and the initial state condition in the theory could be loosened.

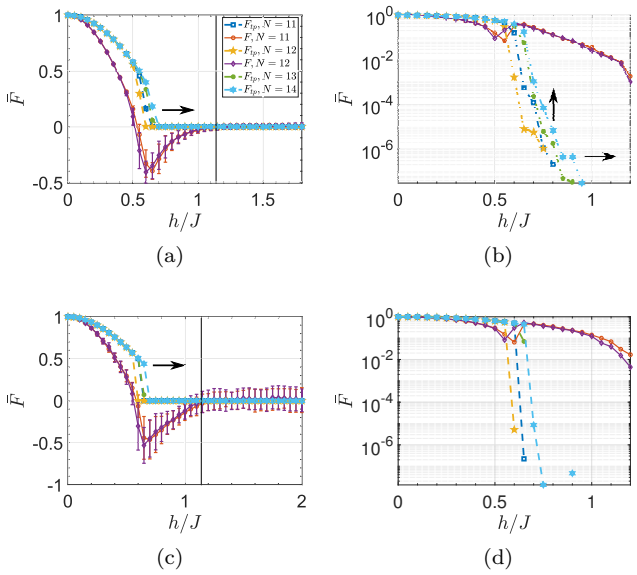

FIG. 10. The finite temperature OTOC saturation F_{∞} (red-circles $N = 11$ and purple-diamonds $N = 12$) and its topological contribution F_{tp} (blue-squares $N = 11$, orange pentagrams $N = 12$, green dots $N = 13$ and light-blue hexagrams $N = 14$) for non-integrable Ising model with $\Delta = 0.1$ [J]. (a)-(b) are for temperature $T = 5$ [J] and (c)-(d) are for $T = 1$ [J] where (a)-(c) are in linear scale and (b)-(d) are in logarithmic scale to demonstrate the decline towards the TPT where no degeneracy is left in the spectrum. All figures are generated for a time interval of $t = 800$ $[1/J]$.

We note that in principle any initial state can reveal this relation as long as the edge operator satisfies the operator ansatz.

B. Zero-energy Modes Localized at the Edge of the Wall

When we drive an edge with an additional constant field in the x-direction, $h_1 = h + 6$ [J] while the rest of the spins have $h_i = h$ [J], we localize the zero-energy mode right at the edge of the wall instead of the edge of the spin chain. Fig. 11 shows the OTOC of edge and the second spins where we moved the zero-energy modes via a constant drive both for integrable and weakly-interacting non-integrable Ising models. We observe how the OTOC of the edge spin now cannot capture the topological order and decays expectantly, whereas the second spin presents almost identical results to our benchmark results discussed in the previous sections. Note that the integrability order persists even for a spin not at the edge of the chain. The blue-circles in Fig. 11b show the integrability effect of matrix elements discussed previously. Additionally the orange-diamonds in Fig. 11b point to the oscillatory OTOC behavior for the edge spin in the integrable model, whereas the oscillations do not persist when we break the integrability in Fig. 11a. In conclusion, the de-

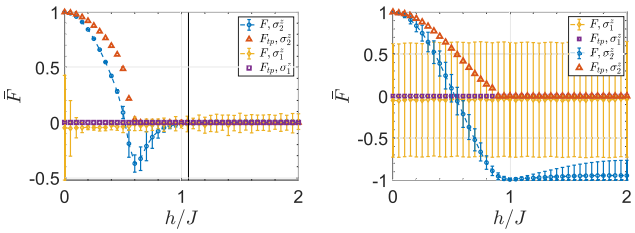

(a) (b)

FIG. 11. The zero-energy mode localized at the second spin (edge of the wall) with a drive field of $h_1 = h + 6$ [J] only applied to the first (edge) spin. (a) The non-integrable Ising model with $\Delta = 0.1$ [J] and (b) the integrable Ising model at $N = 13$: When the OTOC saturation is calculated with an edge spin σ_1^z (F_∞ blue-circles and F_{tp} with red-triangles) and the bulk spin σ_2^z where the zero-energy modes are expected to localize (F_∞ orange-diamonds and F_{tp} with purple-squares). The OTOC decays to zero for the edge spin operator σ_1^z, since the zero-energy modes are not localized at the edge of the chain when the boundary is driven.

tection of topological order via OTOCs demonstrates robustness against the change in the boundary conditions.

V. CONCLUSIONS AND DISCUSSIONS

We put forward an interesting numerical observation on the XXZ model, where we showed the infinite-temperature OTOC, namely a correlator that probes the quantum chaos in interacting many-body systems, is also susceptible to ground-state phase transitions. We proved that its origin is Majorana edge modes existing in the system with a systematic study of first the integrable and then the non-integrable Ising models. The integrable Ising model provided us the opportunity to study the topological contribution to OTOC saturation value analytically and from different perspectives. The integrability order appeared in the OTOC saturation value of the integrable Ising model encouraged us to break the integrability and hence study the effect of interacting Majorana edge fermions. We found that the OTOC saturation value at any temperature, but more fascinatingly at infinite temperature, can detect both the topological order and the TPTs up to finite-size effects. Increasing the interaction strength delocalizes the Majorana zero-energy modes and the topological order that can be captured for finite sizes might not be visible for a system in the thermodynamic limit. Our conclusions in principle can be generalized to higher dimensions for topological states with similar fraction excitations and topological degeneracy, although the numerical verification is yet to be found.

In principle, this probe allows experimental detection of quantum phase transitions and topological states without a need to cool down the system to ultra-low temperatures whether it is the OTOCs, Eq. 8 or two-point correlators, Eq. 16 [27]. In particular, the infinite-temperature OTOCs are experimentally more appealing to zero-temperature OTOCs [48], since it can be challenging to prepare a ground state as the initial state in certain experimental platforms.

The interplay between information scrambling and topological order, though just started to be explored, is an intuitive one. It is well known that the entanglement entropy of a ground state has a universal topological contribution in topologically non-trivial phases [45, 49, 50]. Moreover, the connection between OTOCs and the entanglement entropy of the time-evolved states has been discussed too [51, 52]. Hence here we make another connection which also relates a dynamical quantity to a static property of the Hamiltonian. Our results render the OTOC saturation value as a useful signature to study the TPTs when the zero-energy modes are localized not only at the edge of a chain but also at the edge of a wall in the bulk. Since the OTOC saturation value stays in the order of $\bar{F} \sim 1$, it shows a restricted operator spreading which in turn protects the locality of the spin operators for some h, where the topological order is dominant in the OTOC saturation. This observation lets us wonder about the potential use of information scrambling when we discuss storing data in topologically protected degrees of freedom [53, 54]. This is an interesting future direction that requires systematic study on how the edge modes affect the information spreading possibly via OTOC wavefronts [12, 15, 21]. In particular, introducing the spatial correlations back to OTOC and studying how information spread is restricted by topological order via spatial-temporal correlations would be an exciting next step at the intersection that we have just started to explore. We emphasize that new robustness tests of OTOC in capturing the topological order could be developed in the future, e.g. answering the question if disorder can enhance the detection of topological order via information scrambling. Answers to such questions could bring closer the exciting idea of topologically-protected quantum memory via localized operators [54] in clean or disordered quantum many-body systems.

Appendix A: Methods Explained

To determine the degeneracy in the spectrum, we need to characterize the uncertainty in energy, ΔE. This means that we define an energy window around each energy level with ΔE as $[E_m - \Delta E, E_m + \Delta E]$ where we assume that the states remain in this window are degenerate with the state whose associated energy is E_m. This process defines an energy resolution and in a way coarse-grains the energy spectrum.

As discussed in Ref. [19], the energy resolution is related to the interval of the time-evolution. Longer time-evolution translates to finer energy resolution, resolving the smallest energy differences in the spectrum, $T\Delta E \sim 1$, where T is the total time of the evolution.

Hence anytime we simulate a system with a finite time interval, we define an energy resolution as $\Delta E = \frac{\pi}{4T}$. In return, the parameter ΔE determines the degenerate subspaces in the spectrum and hence helps us to determine the F_{tp}^{∞} contribution (sometimes called as the topological OTOC in the main text) in the OTOC saturation value. Note that this reverse relation between the time interval and energy resolution also implies that any degeneracy lifting (possibly due to finite-size) will be eventually captured by a long-time evolution.

We prefer calling an equation derived by the dynamical decomposition as a framework equation. If the operator in the eigenbasis $W_{\alpha,\beta}$ can be calculated analytically for an integrable system, that would present us the analytical expression of its OTOC saturation value. However, one can numerically derive the matrix elements $W_{\alpha,\beta}$ too and use them in the framework of dynamical decomposition. Any brute force calculation of the OTOC saturation value requires an estimation on the time-dependent part in the dynamical Eq. 6, e.g. which energy pairs are equal to each other. The energy resolution ΔE is used here to define a threshold so that we could exert the degenerate subspaces on the OTOC calculation. Crudely speaking, this threshold determines whether the saturation value is contributed by the found energy set $\left\{E_{[\kappa,\tau]}, E_{[\theta,\alpha]}, E_{[\phi,\gamma]}, E_{[\phi',\gamma']}\right\}$.

When we numerically calculate the OTOC saturation value, we do the summations in Eq. 1. This introduces an approximation to the final OTOC saturation value in our numerical result. We set a threshold where any term greater than the threshold is found and summed over. We determine our threshold based on the dimension of the Hilbert space, $\sim 1/d^2$, where d is the dimension of the Hilbert space. This generally bounds the error on the order of $\sim 10^{-2}$ (we remind the reader that $|F| \leq 1$). This approximation is the reason why the line with red-squares in Fig. 2c slightly diverges from the line with blue-circles.

We utilize ITensor platform in C++ environment and MPS (matrix product states) for our density matrix renormalization group (DMRG) computations [55]. To prepare infinite temperature states in MPS format, we make use of randomly-set Fock states instead of summing over the whole basis. As shown [15], a small number of randomly-set Fock states are able to generate the exact OTOC results up to errors around $\sim 10^{-2}$. We restrict the bond numbers to $m \lesssim 60$. Since the bond numbers increase as the system evolves in time, this results less accuracy for the later times. Therefore, we restrict our time-evolution with MPS to $t \lesssim 5$ [1/J] for $h \geq 1$.

[1] Y. Sekino and L. Susskind, Journal of High Energy Physics **10**, 065 (2008), arXiv:0808.2096 [hep-th].
[2] N. Lashkari, D. Stanford, M. Hastings, T. Osborne, and P. Hayden, Journal of High Energy Physics **4**, 22 (2013), arXiv:1111.6580 [hep-th].
[3] B. Swingle and D. Chowdhury, Phys. Rev. B **95**, 060201 (2017), arXiv:1608.03280 [cond-mat.str-el].
[4] K. Hashimoto, K. Murata, and R. Yoshii, Journal of High Energy Physics **10**, 138 (2017), arXiv:1703.09435 [hep-th].
[5] M. Grttner, J. Bohnet, A. Safavi-Naini, M. L. Wall, J. J. Bollinger, and A. Rey, *Nature Physics*, **13** (2016).
[6] S. H. Shenker and D. Stanford, Journal of High Energy Physics **2014**, 67 (2014), arXiv:1306.0622 [hep-th].
[7] Y. Sekino and L. Susskind, Journal of High Energy Physics **2008**, 065 (2008).
[8] J. Maldacena, S. H. Shenker, and D. Stanford, Journal of High Energy Physics **2016**, 106 (2016).
[9] J. Li, R. Fan, H. Wang, B. Ye, B. Zeng, H. Zhai, X. Peng, and J. Du, Phys. Rev. X **7**, 031011 (2017).
[10] X. Chen, T. Zhou, D. A. Huse, and E. Fradkin, Annalen der Physik **529**, 1600332.
[11] A. Bohrdt, C. B. Mendl, M. Endres, and M. Knap, New Journal of Physics **19**, 063001 (2017), arXiv:1612.02434 [cond-mat.quant-gas].
[12] S. Xu and B. Swingle, arXiv e-prints , arXiv:1802.00801 (2018), arXiv:1802.00801 [quant-ph].
[13] Y. Huang, Y.-L. Zhang, and X. Chen, Annalen der Physik **529**, 1600318 (2017).
[14] R.-Q. He and Z.-Y. Lu, Physical Review B **95**, 054201 (2017), arXiv:1608.03586 [cond-mat.dis-nn].
[15] C. B. Dağ and L. M. Duan, arXiv e-prints , arXiv:1807.11085 (2018), arXiv:1807.11085 [quant-ph].
[16] C.-J. Lin and O. I. Motrunich, Phys. Rev. B **97**, 144304 (2018).
[17] E. Iyoda and T. Sagawa, Phys. Rev. A **97**, 042330 (2018).
[18] H. Shen, P. Zhang, R. Fan, and H. Zhai, Phys. Rev. B **96**, 054503 (2017).
[19] C. B. Dağ, K. Sun, and L. M. Duan, arXiv e-prints (2019), arXiv:1902.05041 [quant-ph].
[20] M. Heyl, F. Pollmann, and B. Dóra, Phys. Rev. Lett. **121**, 016801 (2018).
[21] D. J. Luitz and Y. Bar Lev, Phys. Rev. B **96**, 020406 (2017).
[22] S. Popescu, A. J. Short, and A. Winter, Nature Physics **2**, 754 (2006).
[23] F. Franchini, *An Introduction to Integrable Techniques for One-Dimensional Quantum Systems, Lecture Notes in Physics, Volume 940. ISBN 978-3-319-48486-0.* (2017).
[24] J. Bao and C.-Y. Zhang, arXiv e-prints , arXiv:1901.09327 (2019), arXiv:1901.09327 [cond-mat.stat-mech].
[25] S. Sachdev, *Quantum Phase Transitions* (Cambridge University Press, 2001).
[26] S. Roy, R. Moessner, and A. Das, Phys. Rev. B **95**, 041105 (2017).
[27] F. J. Gómez-Ruiz, J. J. Mendoza-Arenas, F. J. Rodríguez, C. Tejedor, and L. Quiroga, Phys. Rev. B **97**, 235134 (2018).
[28] Y. Wang, Phys. Rev. E **98**, 042128 (2018).
[29] M. D. Caio, N. R. Cooper, and M. J. Bhaseen, Phys. Rev. Lett. **115**, 236403 (2015).
[30] J. Yu, Phys. Rev. A **96**, 023601 (2017).

[31] Y. Hu, P. Zoller, and J. C. Budich, Phys. Rev. Lett. **117**, 126803 (2016).

[32] N. Fläschner, D. Vogel, M. Tarnowski, B. S. Rem, D.-S. Lühmann, M. Heyl, J. C. Budich, L. Mathey, K. Sengstock, and C. Weitenberg, Nature Physics **14**, 265 (2018).

[33] L. D'Alessio and M. Rigol, Nature Communications **6**, 8336 (2015), arXiv:1409.6319 [cond-mat.quant-gas].

[34] M. McGinley and N. R. Cooper, Phys. Rev. B **99**, 075148 (2019).

[35] A. Kitaev, AIP Conference Proceedings **1134**, 22 (2009).

[36] M. Heyl, A. Polkovnikov, and S. Kehrein, Phys. Rev. Lett. **110**, 135704 (2013), arXiv:1206.2505 [cond-mat.stat-mech].

[37] J. C. Budich and M. Heyl, Phys. Rev. B **93**, 085416 (2016).

[38] M. Schmitt and S. Kehrein, Phys. Rev. B **92**, 075114 (2015).

[39] A. Y. Kitaev, Physics Uspekhi **44**, 131 (2001), arXiv:cond-mat/0010440 [cond-mat.mes-hall].

[40] M. Srednicki, in *eprint arXiv:chao-dyn/9511001* (1995).

[41] M. Srednicki, Journal of Physics A Mathematical General **32**, 1163 (1999), cond-mat/9809360.

[42] M. Rigol, V. Dunjko, and M. Olshanii, Nature (London) **452**, 854 (2008), arXiv:0708.1324 [cond-mat.stat-mech].

[43] L. D'Alessio, Y. Kafri, A. Polkovnikov, and M. Rigol, Advances in Physics **65**, 239 (2016), arXiv:1509.06411 [cond-mat.stat-mech].

[44] C. Gogolin and J. Eisert, Reports on Progress in Physics **79**, 056001 (2016), arXiv:1503.07538 [quant-ph].

[45] H.-C. Jiang, Z. Wang, and L. Balents, Nature Physics **8**, 902 (2012), arXiv:1205.4289 [cond-mat.str-el].

[46] D.-J. Zhang and J. Gong, Phys. Rev. A **98**, 052101 (2018).

[47] K. A. Landsman, C. Figgatt, T. Schuster, N. M. Linke, B. Yoshida, N. Y. Yao, and C. Monroe, ArXiv e-prints (2018), arXiv:1806.02807 [quant-ph].

[48] Z.-H. Sun, J.-Q. Cai, Q.-C. Tang, Y. Hu, and H. Fan, arXiv e-prints , arXiv:1811.11191 (2018), arXiv:1811.11191 [quant-ph].

[49] A. Kitaev and J. Preskill, Phys. Rev. Lett. **96**, 110404 (2006).

[50] M. Levin and X.-G. Wen, Phys. Rev. Lett. **96**, 110405 (2006).

[51] R. Fan, P. Zhang, H. Shen, and H. Zhai, Science Bulletin **62**, 707 (2017).

[52] C. W. von Keyserlingk, T. Rakovszky, F. Pollmann, and S. L. Sondhi, Phys. Rev. X **8**, 021013 (2018).

[53] R. Nandkishore and D. A. Huse, Annual Review of Condensed Matter Physics **6**, 15 (2015).

[54] D. A. Huse, R. Nandkishore, V. Oganesyan, A. Pal, and S. L. Sondhi, Phys. Rev. B **88**, 014206 (2013).

[55] ITensor Library (version 2.0.11) http://itensor.org.